FINAL TECHNICAL REPORT

DOE Award Number: DE-SC0002197

DOE/Office of Science Program Office: Basic Energy Sciences (BES)

Project title: Combined microscopy studies of complex electronic materials

Recipient Institution: University of Washington, Seattle

Principle Investigator: David H. Cobden (sole PI)
Period of Performance: 09/15/2009 - 06/14/2019

ABSTRACT

The aim of this project was to study the electronic properties of exotic electronic materials which are only available as micron-scale samples or have microscopic inhomogeneity, using a special combination of multiple submicron scanning microscopy techniques allied to control of temperature, magnetic and electric fields and mechanical strain. In nanobeams of VO_2, with its still mysterious metal-insulator phase transition, we determined the phase diagram and demonstrated that hydrogen diffusion is strongly channelled along one crystal axis. Using graphene, we developed and applied the scanning photo-Nernst effect, in which a current is generated when a laser is focused on the edge a sample in a magnetic field. We demonstrated that CrI_3, a two-dimensional layered magnet, retains true Ising ferromagnetization down the monolayer level due to its out-of-plane anisotropy. In exfoliated WTe_2, a layered topological semimetal, we discovered that monolayers are the first monolayer topological insulator and we imaged the helical edge states with scanning microwave microscopy. We also discovered that the same material when stacked in a few layers is a ferroelectric metal, and that the monolayer can be converted to a superconducting state by electron doping with a gate a temperatures below 1 K. Additionally, we developed the capability to perform momentum-resolved electronic spectroscopy on operating nanoscale devices by applying micron-scale angle resolved photoemission spectroscopy to two-dimensional heterostructure devices incorporating graphene and transition metal dichalcogenide semiconductors. Using it, we measured the band gaps of a series of monolayer semiconductors and observed band renormalization as a function of electron doping in monolayer WSe_2.

SUMMARY OF PROJECT ACTIVITES

1. The metal-insulator transition in VO_2

Significant results were obtained in a number of materials systems, we organize the results by system.

In the first-order metal-insulator transition (MIT) in VO_2, which involves strong correlations between electrons and phonons, multiple insulating phases (M1, M2 and T) compete with the metallic phase (R) as temperature is lowered. Such first-order transitions in solids are challenging to study because of the combination of change in unit cell shape, the long range of elastic distortion, and the flow of latent heat, which lead to domain structure, nonuniform strain, hysteresis, and often cracking. To avoid these problems we developed a nanomechanical strain microscope, affording the unique ability to precisely control both temperature and axial stress in a nanobeam or nanowire. In our early work we established for the first time the equilibrium phase boundaries in VO_2 (Fig. 1a) and found that the triple point of the R, M1 and M2 phases is at $T_{tr} = T_c = 65.0 \pm 0.1$ °C and at zero strain (https://arxiv.org/abs/1308.4741). With electrical contacts we also determined the strain dependence of the M1 phase resistivity and detected the triclinic

distortion of M1. The findings have important implications for the mechanisms of the MIT in VO_2 and other oxides, and demonstrate the value of this approach for mastering phase transitions in complex materials.

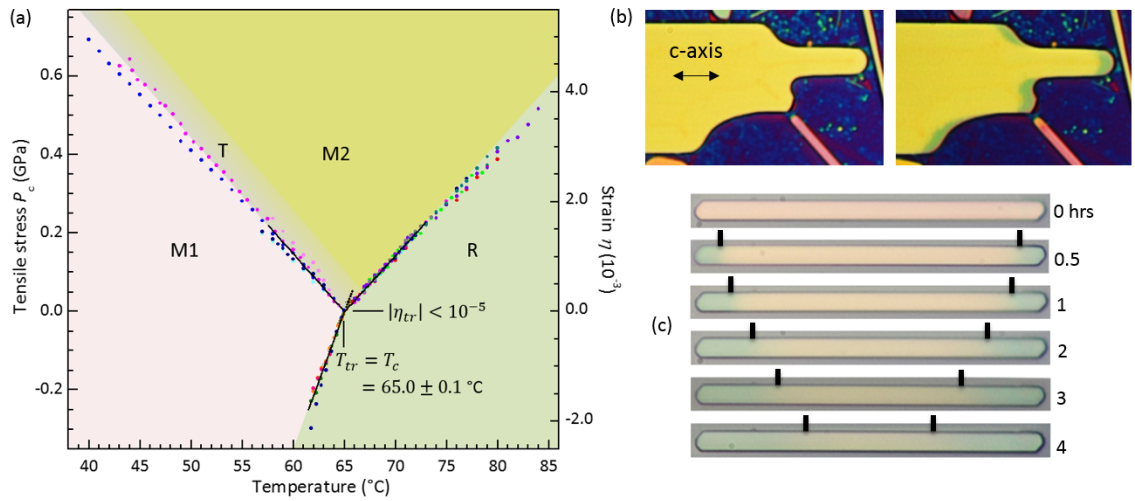

Figure 1. (a). The equilibrium stress-temperature phase diagram of VO_2 near the the metal-insulator transition, established using our nanomechanical strain setup incorporating optical microscopy and electrical transport. (b) Optical images of a VO_2 platelet at room temperature, as-grown (left), and after exposure to hydrogen gas at 100 °C for 15 minutes (right). The anisotropy of hydrogen diffusion is evident in the pattern of darker, doped regions here. The image width is 50 µm. (c) Images of one nanobeam (width 5 microns) after different hydrogen exposure times. From these the diffusion coefficient along the c-axis at 100 °C is determined to be 2×10^{-11} cm^2/s.

We also studied the ultrafast induction of the MIT on the nanoscale in collaboration with Markus Raschke, University of Colorado (https://arxiv.org/abs/1412.5495).

The diffusion of hydrogen in solids is common and has many ramifications but is poorly understood. It is strongly affected by inhomogeneity such as grain boundaries and strain, and is also difficult to monitor. Hydrogen in VO_2 changes the activation gap, MIT temperature, and color, allowing one to visualize its diffusion with optical microscopy. We exploited this to investigate the diffusion of hydrogen in VO_2 in suspended single-crystal VO_2 nanobeams (https://arxiv.org/abs/1606.08311). We determined that diffusion is orders of magnitude faster along the c-axis, as illustrated in Figs. 1b and c.

2. Photo-Nernst effect in graphene

As a focused laser spot, or a tip scattering light, is scanned the spatial variation of the photocurrent gives insights into the electronic processes, on a submicron scale, and this can be done on small samples or domains with a moderate amount of preparation involving attachment of just two contacts. Scanning photocurrent microscopy can readily be performed at low temperatures, high magnetic fields, and on a stage which allows strain application. In developing this technique in collaboration with Xiaodong Xu at the University of Washington we worked with simple and convenient graphene samples (Fig. 2a). At zero magnetic field photocurrent is of a photoelectric nature, the electrons rapidly reaching local thermal equilibrium under the laser spot leading to a temperature gradient within the sample. We found that in a perpendicular magnetic field B additional photocurrent is generated when the laser spot is near a free edge, with opposite sign at opposite edges and antisymmetric in B (Fig. 2b). We explained this as resulting from the

Nernst effect (https://arxiv.org/abs/1510.00765), combined with the Shockley-Ramo nature of long-range photocurrent generation in a gapless material.

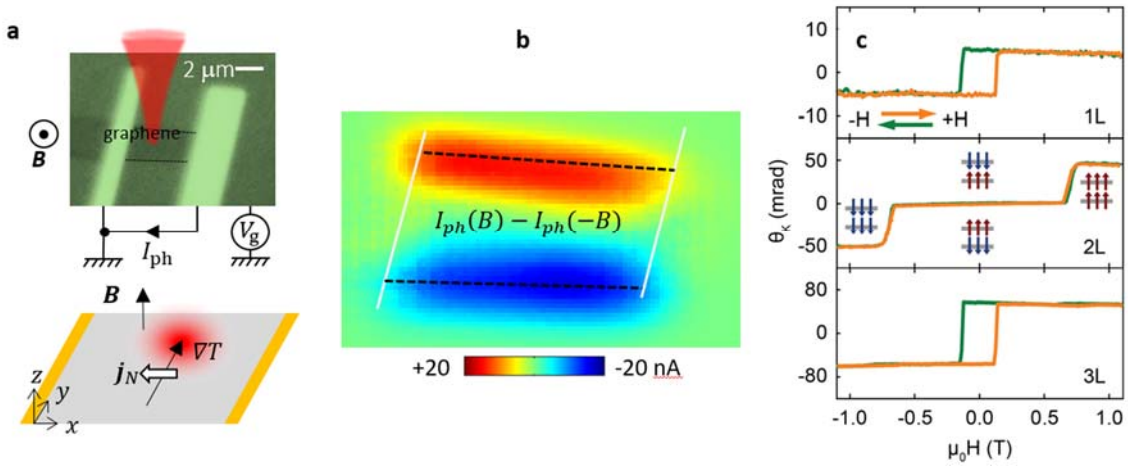

Figure 2. (a) the Photo-Nernst effect in a graphene device involves focusing a scanned laser spot on the sample in a perpendicular magnetic field. The temperature gradient around the laser combined with the magnetic field produces a Nersnt effect which is large only when the laser is near the free sample edges, indicated by the dashed lines in the photocurrent image (b). Here the Nernst component is separated out by plotting the B-antisymmetric part of the photocurrent. (c) Kerr rotation in monolayer, bilayer and trilayer CrI_3 as indicated, demonstrating the layered antiferromagnetic behavior at temperature 2 K.

3. CrI_3, the first monolayer magnet

In collaboration with Xiaodong Xu at the University of Washington we studied exfoliated layered magnets. We succeeded in demonstrating using Kerr microscopy that CrI_3 has intralayer out-of-plane ferromagnetism at temperatures below ~45 K in the monolayer and interlayer antiferromagnetism (Fig. 2c) (https://arxiv.org/abs/1703.05892). We also observed giant tunneling magnetoresistance in tunnel structures incorporating hBN barriers. This occurs due to the adjacent layers of the CrI acting as spoin filters for the tunneling electrons. At low external field they are antialigned and the current is small; at higher field (around 1 T) a spin-flop transition occurs and the current jumps by orders of magnitude (https://arxiv.org/abs/1802.06979). We also demonstrated electrical control of the spin-flop field (https://arxiv.org/abs/1802.06979) using gate electrodes, which involves charge transfer from a graphene electrode into the magnetic material.

4. Discovery of the first natural 2D topological insulator, monolayer WTe_2

In a major thrust, we succeeded in producing well behaved heterostructures incorporating air-sensitive 2D materials, including WTe_2 as well as several magnets. It was predicted earlier that WTe_2, which is a semimetal in 3D, might become a 2D topological insulator in monolayer form. We found that the monolayer indeed exhibits the characteristics of a topological insulator (https://arxiv.org/abs/1610.07924). At low temperatures there is a ~50 meV gap for conductivity in the 2D bulk, while the edges remain conducting, consistent with topologically protected boundary modes. The edge conductivity is suppressed by an in-plane magnetic field, consistent with increased backscattering in helical edge modes when time reversal symmetry is broken.

Figure 3a shows characteristics of 3-, 2- and 1-layer exfoliated WTe_2 sheet encapsulated in hBN with graphite gates above and below; the gate voltage V_g is applied to both gates. Only the monolayer shows a plateau of edge conduction at low V_g. The bilayer was expected to be topologically trivial and thus not have boundary modes, as seen to be the case. For 3+ layers the

material is always metallic. The conductance of the plateau is below e^2/h in all devices, implying that some backscattering occurs and/or contacts are imperfect, for reasons still being explored. Proof of edge conduction came not only from transport measurements but also from microwave impedance microscopy (MIM) measurements (Fig. 3b) performed in collaboration with Yongtao Cui at UC Riverside (https://arxiv.org/abs/1807.09342). MIM yielded important insights, such as revealing how the topological edge mode conforms to tiny cracks in the edges as can be seein in the bottom left image.

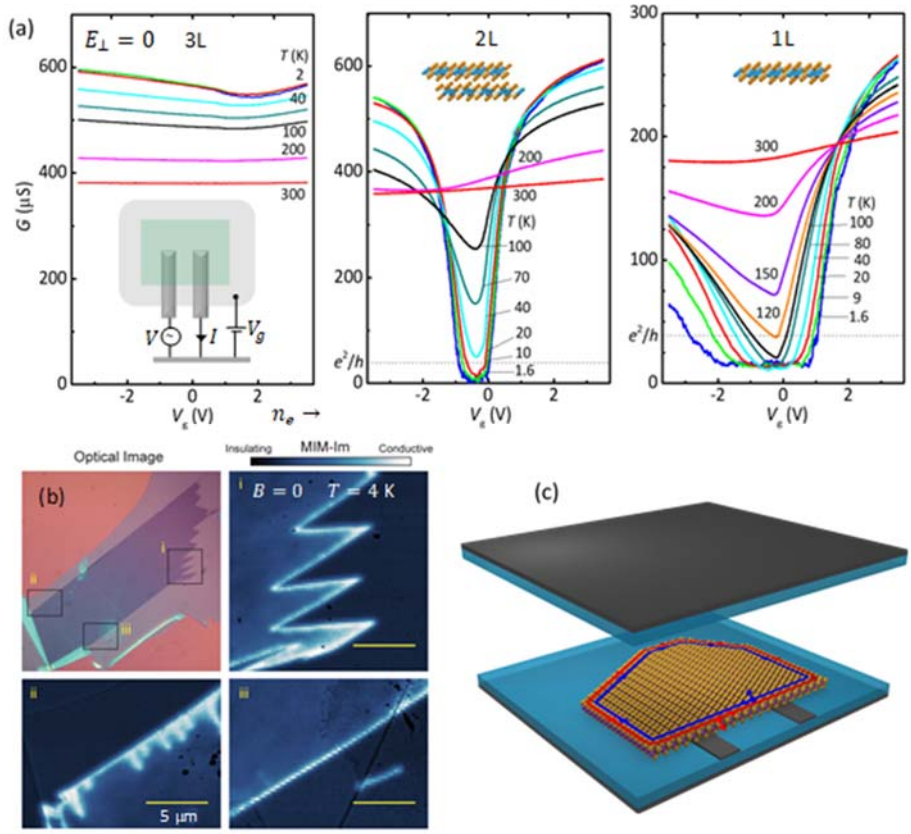

Figure 3. (a) Gate and temperature dependence of the two-probe conductance for (left) trilayer, (center) bilayer, and (right) monolayer WTe_2. The trilayer is metallic; the bilayer is insulating at $V_g = 0$ but metallic when n- or p-doped using the gates; and the monolayer has a plateau of conduction below ~100 K where the current only flows along the sample edges while the 2D bulk becomes insulating at low gate voltages. (b) Microwave impedance microscopy (MIM) images of a large monolayer WTe_2 flake protected by an even large hBN sheet (optical image, top left). (In collaboration with Yongtao Cui, UC Riverside). The edges are conducting (bright) while the 2D bulk is insulating (dark) as is the surrounding SiO_2 substrate. (c) Schematic showing the helical edge states and the graphene/hBN sandwich which encapsulates the air-sensitive WTe_2 flake as well as the Pt contacts.

Surprisingly, we found that the 2D bulk of the monolayer changes from insulating to a superconducting state under a positive gate voltage, as shown in Fig. 4a, at temperatures below about 1 K (in collaboration with Joshua Folk, University of British Columbia) (https://arxiv.org/abs/1809.04691). The transition is very broad, as expected since the normal state areal conductivity is not much higher than e^2/h. The intermediate plateau is not understand. Suppression of the superconductivity by a perpendicular magnetic field occurs on a scale of 30 mT, giving a coherence length of ~100 nm. Suppression by an in-plane field occurs on a scale of 3 T, about twice the expected Pauli pair-breaking limit assuming a g-factor of 2. Figure 4b shows

a phase diagram extracted from the measurements, where the x-axis is the doping density determined from the capacitance. It is particularly striking that the transition from 2DTI to 2D superconductor occurs at an electron doping level of only $\sim 5 \times 10^{12}$ cm^{-2}, an order of magnitude lower than in other doping-induced superconducting transitions in similar 2D materials.

We further discovered that bilayer and trilayer WTe_2 exhibit a spontaneous out-of-plane electrical polarization (https://arxiv.org/abs/1809.04575), allowed by the known crystal symmetry (Fig. 4c). This polarization can be reversed by applying an electric field, that is, the material is ferroelectric.

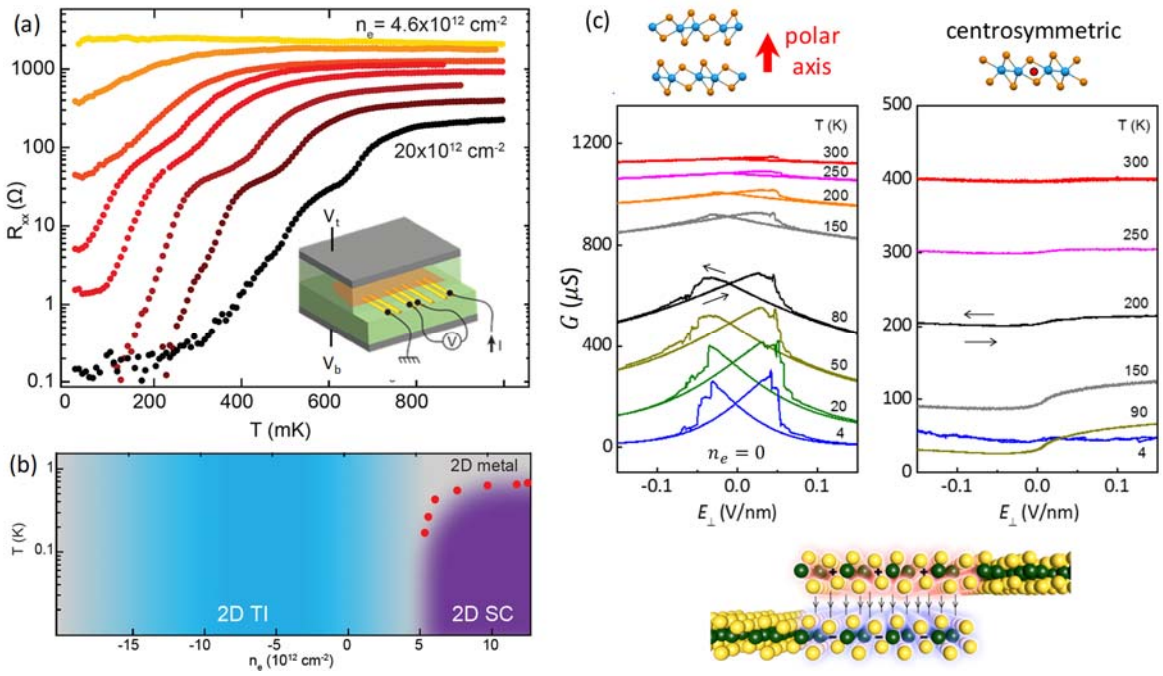

Figure 4. Superconductivity and ferroelectricity in WTe_2. (a) Temperature dependence of four-terminal resistance of a monolayer WTe_2 device, measured as indicated in the inset, at a series of gate voltages. The electron doping density n_e, shown, is determined from the geometric capactitance. (b) Deduced phase diagram. The insulator-superconductor boundary (red dots) is taken to be the point where the the resistance is half that in the normal (high temperature) tate. (c) Ferroelectric switching in bilayer and monolayer WTe_2 devices. The bilayer (left) has polar structure and its polarization can be flipped by applying a perpendicular electric field by putting opposite-sign voltages on the top and bottom gates. The monolayer (right) is centrosymmetric and cannot be flipped. Spontaneous polarization occurs when the monolayers are stacked, as indicated in the cartoon below.

5. Angle-Resolved Photoemission Spectroscopy (μ-ARPES) on operating 2D devices

Finally, we developed the capability to perform ARPES on 2D materials, in collaboration with Neil Wilson at the University of Warwick and using the Spectromicroscopy beamline at Elettra in Trieste. We established the band parameters of monolayer $MoSe_2$ and WSe_2 and their heterobilayers (https://arxiv.org/abs/1601.05865). Subsequently, we achieved the first in-situ electrostatic gating carried out during photoemission spectroscopy (https://arxiv.org/abs/1904.07301). The gate-doping of graphene is illustrated in Fig. 5a, and of monolayer semiconductor WSe_2 in Fig. 5b.

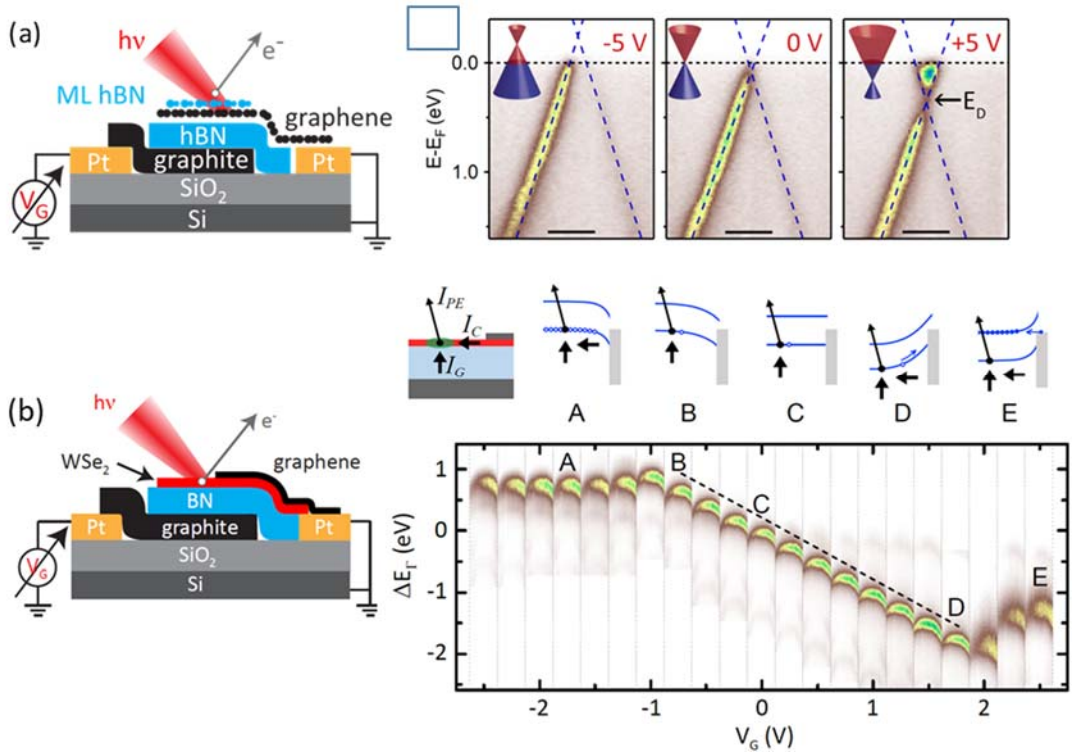

Figure 5. In-situ gating of 2D devices in μ-ARPES. (a) The sample geometry is similar to a standard operating graphene field-effect transistor. A gate voltage is applied to dope the graphene while performing photoemission (27 eV photons, 1 μm beam spot.) On the right are E-k momentum slices close to the graphene K-point at different indicated gate voltages, showing the expected conical (massless Dirac) dispersion (the dashed lines are fits). (b) For semiconductor studies, a semiconducting flake of, say, monolayer WSe_2 is incorporated into the stack with the top graphee used as a contact (left). The right hand panel shows the effect of gate voltage on the valence band edge at Γ, with band diagrams above indictating the situation at each marked point.

Disclaimer: This report was prepared as an account of work sponsored by an agency of the United States Government. Neither the United States Government nor any agency thereof, nor any of their employees, makes any warranty, express or implied, or assumes any legal liability or responsibility for the accuracy, completeness, or usefulness of any information, apparatus, product, or process disclosed, or represents that its use would not infringe privately owned rights. Reference herein to any specific commercial product, process, or service by trade name, trademark, manufacturer, or otherwise does not necessarily constitute or imply its endorsement, recommendation, or favoring by the United States Government or any agency thereof. The views and opinions of authors expressed herein do not necessarily state or reflect those of the United States Government or any agency thereof."